Catalysis
Science &
Technology

rsc.li/catalysis

Volume 7
Number 2
21 January 2017
Pages 313–534

ISSN 2044-4761

ROYAL SOCIETY
OF CHEMISTRY

PAPER
Chaoqiu Chen, Yong Qin et al.
Highly dispersed Pt nanoparticles supported on carbon
nanotubes produced by atomic layer deposition for hydrogen
generation from hydrolysis of ammonia borane

ROYAL SOCIETY
OF CHEMISTRY

rsc.li/catalysis

ARTICLE

Theoretical insights on hydrogen activation and diffusion behaviour on ZnO (10$\bar{1}$0) surface

Zezhong Miao,[ab] Xing Zhu,[c] Yuqian Jin,[d] Lingzhao Kong,*[c] and Shenggang Li *[ab]

ZnO is an important component in many catalysts for hydrogenation of carbon monoxide and dioxide, upcycling of plastics and hydrodeoxgenation of biomass, which exhibits a strong capacity for H_2 activation. This work examines eleven distinct H_2 activation pathways on pristine and defective ZnO (10$\bar{1}$0) surfaces, demonstrating that the OV-Zn_3 ensemble is not a spectator site. Instead, OV-Zn_3 acts as an electron reservoir with strong electron-donating ability albeit with limited electron-storage capacity. This region interacts with surface H adsorbates and, while modulating the behavior of the adsorbed H species, undergoes lattice distortion and electronic rearrangement as the adsorption site varies. Furthermore, the tendency of the H atoms to adsorb on the Zn-O pairs drives the growth of an one-dimensional H-chain along the [0001] direction, leading to distinct diffusion behavior along the [0001] and [1$\bar{2}$10] directions. The existence of multiple H_2 activation routes and H diffusion pathways provides a rational explanation for the experimentally observed variations in the OV concentration as well as the hydrogen coverage at the OV sites. By correlating these atomic-scale insights with available experimental observations, we propose how defect engineering and thermal control could be synergistically employed to tune H_2 activation on ZnO surfaces, providing a fresh perspective for rational catalyst design of ZnO-based hydrogenation catalysts.

1 Introduction

Utilizing renewable H_2 to convert CO/CO_2 into high-value products[1-3] is an important part of the CCUS (Carbon Capture, Utilization and Storage) technology[4, 5]. ZnO-based catalysts such as $Zn_xCr_yO_z$[6], $Zn_xZr_yO_z$[7], $Zn_xGa_yO_z$[8], $Zn_xAl_yO_z$[9], $Zn_xIn_yO_z$[10], $Zn_xMn_yO_z$[11], and $Zn_xFe_yO_z$[12], are widely used for CO_2 hydrogenation to methanol, syngas conversion into light olefins and water-gas shift reaction. ZnO-based catalysts also play a key role in plastics upcycling[13-15] and biomass hydrodeoxygenation conversion[13, 16, 17]. Despite major advances, there remain debates on the reaction mechanism owing to the structural complexity of the catalysts and the multitude of adsorbates and intermediates involved.

Recent studies indicate that the ZnO component in these catalysts often plays a decisive role in H_2 activation. For Cu/Zn/Al_2O_3, which is the mature industrial methanol synthesis catalyst,[18] the Cu/ZnO interface or CuZn alloy has been widely recognized as the primary active site[2, 19]. H_2 molecules are believed to dissociate at the ZnO/Cu interface with a relatively low energy barrier and subsequently spillover to terminal

oxygen atoms on the ZnO surface, contributing to oxygen vacancy (OV) formation[20]. For $ZnZrO_x$ solid solution catalyst, Zn-O pairs have been identified as the main active sites for heterolytic H_2 dissociation[21, 22]. Similarly, on the surface of $ZnAl_2O_4$ spinel catalysts, the formation of an amorphous ZnO phase is believed to facilitate H_2 activation, thereby enhancing the methanol production rate[23]. Effective H_2 activation not only provides the necessary hydrogen for subsequent reactions but also promotes the formation of OVs, which can serve as highly active sites for CO_2 activation[24].

Liu et al. constructed an inverse Ni–ZnO interface with interfacial frustrated Lewis pairs capable of heterolytically cleaving H_2 into $H^{\delta+}/H^{\delta-}$ and thereby accelerating carbonyl hydrogenation[25]. A Ni_1Fe_1–ZnO interface was engineered to enable quantitative conversion of methyl stearate by hydrogenation to octadecanol with 92.7% selectivity and an initial rate three times higher than NiFe/C[26]. In addition, for polyol hydrogenolysis (e.g., glycerol to 1,2-propanediol), ZnO in the classic Cu–ZnO catalytic systems serves as an "atomic-hydrogen reservoir", which promotes hydrogen spillover, as it can promote both H_2 activation and hydrogen transfer steps required for selective hydrogenolysis[27]. ZnO by itself possesses an inherently high capacity for H_2 activation, which is well suited for use as H_2 gas sensors[28-30] for detecting leaks in hydrogen fuel storage systems[31]. Even at temperatures as low as 20 K, H_2 can dissociate and form one-dimensional (1D) hydrogen chains aligned along the [0001] direction on the ZnO (10$\bar{1}$0) surface[32]. Infrared study[33] and theoretical calculations[34, 35] have demonstrated that H_2 activation on the ZnO (10$\bar{1}$0) surface proceeds via heterolytic dissociation at Zn-O pairs, forming a hydride (H-Zn) and a hydroxyl (O-H).

[a.] Low-Carbon Conversion Science and Engineering Centre, and State Key Laboratory of Low Carbon Catalysis and Carbon Dioxide Utilization, Shanghai Advanced Research Institute, Chinese Academy of Sciences, Shanghai 201210, China. E-mail: lisg@sari.ac.cn.

[b.] School of Physical Science and Technology, ShanghaiTech University, Shanghai 201210, China.

[c.] School of Environmental Science and Engineering, Suzhou University of Science and Technology, Suzhou, Jiangsu, 215009, P.R. China. E-mail: konglz@sari.ac.cn.

[d.] Department of Chemistry, University of California, Irvine, Irvine, CA 92697, USA.

† Supplementary Information available: [details of any supplementary information available should be included here]. See DOI: 10.1039/x0xx00000x

Activated hydrogen species can readily diffuse on the ZnO ($10\bar{1}0$) surface, both along [0001] and [$1\bar{2}10$]. Hydrogen atoms adsorbed on Zn have been observed to migrate to adjacent O atoms[34, 36]. However, DFT calculations[34] indicate that migration to neighbouring O_{4c} and O_{3c} sites has reaction energies of 0.09 eV and −0.01 eV, respectively, with activation barriers of 1.40 eV and 1.10 eV. The final states are not thermodynamically more stable than the initial states, and the kinetic barriers are relatively high, which together do not strongly support this scenario. Recently, Ling et al. observed hydrogen diffusion along the [$1\bar{2}10$] direction[37], where the atomic rows are composed solely of either Zn or O atoms (Fig. 1a) rather than alternating Zn-O pairs. However, the driving force and mechanism governing the diffusion across identical atomic sites remain unresolved.

OVs have also been experimentally identified on ZnO surfaces[38]. Although Ling et al. previously proposed that H_2 dissociation on ZnO surfaces proceeds without assistance of OVs[37], recent studies indicate that the contribution of these defects to H_2 activation remains largely overlooked. Song et al. exposed ZnO to H_2 at 200 °C and detected a single resonance at 8.4 ppm in the ^{1}H MAS-NMR spectrum[34]. They unequivocally attributed it to hydrogen species adsorbed at OVs. This finding provides evidence for the probability of H_2 dissociation at these defect sites. Subsequent experiments[36] tracked how the coverages of OVs and hydrogen species on the ZnO ($10\bar{1}0$) surface evolve with temperature under an H_2 atmosphere: at 40 °C, heterolytic H_2 dissociation on the stoichiometric surface dominated with no OVs observed; at 150 °C, vacancies began to form, but no hydrogen signal associated with them was detected; at 200 °C, more OVs were generated from a deeper reduction, which became populated by hydrogen, so the net vacancy concentration did not rise markedly relative to that of 150 °C; at 300 °C, both the OV density and the coverage of vacancy-bound hydrogen decreased, ascribed to migration of lattice oxygens from the bulk to the surface.

In this work, we elucidate the mechanism by which an OV–Zn_3 motif forms on ZnO ($10\bar{1}0$) surfaces. We further examined eight distinct chemisorption configurations for atomic hydrogen and eleven for molecular H_2 on the ZnO surface to probe multiple modes of interaction between hydrogen species and the surface, as well as their impact on lattice distortion, a powerful lever for tuning catalytic performance.[39] In addition, we investigate the self-assembly of H species into 1D hydrogen chains and their surface diffusion. Viewed from the behaviour of H species, our analysis offers a possible explanation for the experimentally observed temperature dependence of OV and hydrogen coverages. These insights are important for the rational design of more effective ZnO-based catalysts.

2 Computational methods

All density functional theory (DFT) calculations were conducted using the Vienna ab initio simulation package (VASP)[40, 41] with the Perdew-Burke-Ernzerhof (PBE) exchange-correlation functional[42] within the generalized gradient approximation (GGA). Core–valence interactions were described by projector augmented wave (PAW)[43, 44] pseudopotentials, and a plane-wave energy cutoff of 500 eV was adopted to ensure the convergence of the calculated energetics. Gaussian smearing with a smearing width of 0.1 eV was used to treat possible partial occupancies. The electronic self-consistent loop was considered converged when the total energy change was smaller than 1×10^{-5} eV, and the structure optimization was considered completed when the residual force on each relaxed atom was less than 0.03 eV/Å. Transition states were located using both the climbing image nudged elastic band (CI-NEB)[45] method and the improved dimer method (IDM)[46, 47] as implemented in VASP. All transition states located were further validated by the presence of one and only one imaginary frequency corresponding to the reaction coordinate. AIMD (ab initio molecular dynamics) simulations were conducted at 300 K. Microkinetic modelling was performed with the CatMAP package[48, 49]. All structures were constructed using Materials Visualizer in Materials Studio[50].

Crystal orbital Hamilton population (COHP) analyses were performed with the LOBSTER package[51]. For each atom pair A–B, the integrated COHP (ICOHP) was computed as:

$$ICOHP_{A-B} = \int_{-\infty}^{E_F} COHP_{A-B}(E)dE$$

In this sign convention, bonding contributions are negative and antibonding positive, so larger −ICOHP (i.e., more negative ICOHP values) indicate a stronger net A–B interaction up to the Fermi level. The charge-density difference as well as electron localization function (ELF) maps were visualized using VESTA[52].

Lattice parameters of the primitive unit cell (PUC) of bulk ZnO (Fig. S1a) were calculated as a = b = 3.29 Å and c = 5.30 Å, compared favourably with their experimental values of a = b = 3.25, and c = 5.21 Å[53]. For the ZnO ($10\bar{1}0$) surface, a periodic supercell of (3 × 2) with 3 repeated layers along the z direction was constructed (Fig. S1 b,e). To eliminate spurious interactions between periodic images, a vacuum region of 15 Å was introduced along the z-direction. A Γ-centered Monkhorst-Pack[54] k-point mesh of (3 × 3 × 1) was employed to sample the Brillouin zone, and a denser (5 × 5 × 1) grid was used for electronic-structure calculations.

The formation energy of a thermally induced OV is defined as the reaction energy for thermal desorption of molecular O_2:

$$\Delta E_{f,t-OV} = E_{slab}^{OV} - E_{slab}^{pristine} + \frac{1}{2}E_{O_2}$$

In addition, the formation energy of a hydrogen-induced OV, with respect to gas-phase H_2/H_2O is defined as:

$$\Delta E_{f,h-OV} = E_{slab}^{OV} - E_{slab}^{pristine} - E_{H_2} + E_{H_2O}$$

In the above equations, E_{slab}^{OV} and $E_{slab}^{pristine}$ are the total energies of the defect and pristine slabs, $E_{O_2}, E_{H_2}, E_{H_2O}$ are the energies of gas-phase O_2, H_2 and H_2O, respectively

The adsorption energy of adsorbate A on a slab is defined as:

$$E_{ad,A} = E_{total} - (E_{slab} + E_A)$$

Here, E_{total} is the total energy of the adsorbate-slab system, E_{slab} is the energy of the clean slab, and E_A is the energy of the isolated adsorbate molecule.
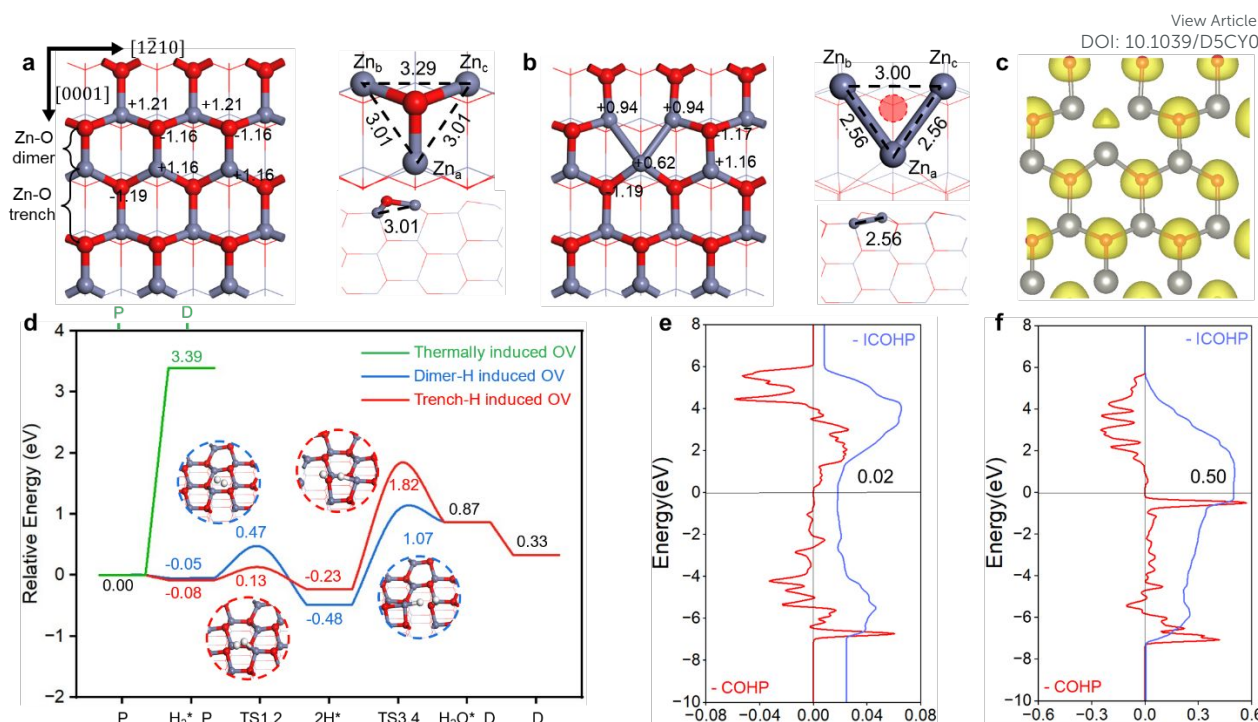
Fig. 1 (a,b) Bader charges and bond lengths for pristine and defect ZnO ($10\bar{1}0$) surfaces, with units of e and Å, respectively. (c) Electron localization function (ELF) map of defect ZnO ($10\bar{1}0$) surface. (d) Potential energy surfaces (PES) of OV formation. (e,f) COHP analyses for the interaction between Zn_a and Zn_b on pristine and defect ZnO ($10\bar{1}0$) surfaces.

3 Results and discussion

3.1 Formation of OV-Zn$_3$ on ZnO ($10\bar{1}0$) surface

The nonpolar ($10\bar{1}0$) facet is the most stable surface of hexagonal wurtzite ZnO[55-57], exposing three-coordinated Zn (denoted as Zn_{3c}) and O (denoted as O_{3c}) atoms (Fig. S1). Atoms in the subsurface and the bulk are four-coordinated and are denoted Zn_{4c} and O_{4c}. As shown in Fig. 1a, a single type of O or Zn atoms are linearly arranged along the $[1\bar{2}10]$ direction. Along the [0001] direction, Zn and O atoms alternate. And there are two types of adjacent Zn-O pairs: one is closer and directly bound as the Zn-O dimer, and the other is more distant, without direct bond formation, resembling a trench, referred to as the Zn-O trench[58]. Here, "dimer-Zn_{3c}" denotes the Zn atom that pairs with a given O_{3c} atom to form a Zn-O dimer, and "trench-O_{3c}" denotes the O atom that pairs with a given Zn_{3c} atom to form a Zn-O trench; "dimer-O_{3c}" and "trench-Zn_{3c}" are defined similarly.

For the O_{3c} atoms on the ZnO ($10\bar{1}0$) surface, the formation energy of a thermally induced OV is 3.39 eV (Fig. 1d), while hydrogen-induced OV formation is thermodynamically much more favourable, with a formation energy of only 0.33 eV. After heterolytic dissociation of H_2 on a Zn-O pair, the H atom adsorbed on Zn_{3c} migrates to the O_{3c} site to form H_2O. The subsequent desorption leaves an OV (Fig. S2). We define OVs generated via H species adsorbed on a Zn-O dimer as dimer-H induced OVs, and those from H adsorbed on a Zn-O trench as trench-H induced OVs. The rate-determining step (RDS) of OV formation is H_2O formation rather than H_2 dissociation. The

energy barriers of the RDS are 1.55 eV and 2.05 eV for dimer-H and trench-H induced OVs formation, respectively, indicating that OV formation is kinetically more favourable when H_2 dissociates on a Zn-O dimer. In contrast, removal of a subsurface O_{4c} atom is more endothermic at 3.84 eV (Fig. S3a). Our AIMD sampling indicates that H species are unlikely to adsorb onto Zn_{4c}-O_{4c} due to the higher endothermicity (Fig. S3b, 3c). Consequently, neither thermally nor hydrogen-induced vacancies are likely to originate from O_{4c}.

ELF analysis (Fig. 1c) reveals charge localization at the OV site, which attracts nearby Zn ions—one on the surface (denoted as Zn_a) and two in the subsurface (denoted as Zn_b and Zn_c, which are symmetry-equivalent). The Zn-Zn distances decrease from 3.01 and 3.29 Å to 2.56 and 3.00 Å, approaching the bond lengths in hexagonally close-packed metallic Zn (2.66 and 2.94 Å, Fig. S1d). The Zn_a-Zn_b interaction is significantly strengthened upon OV formation, as indicated by an increase in the -ICOHP value from 0.02 eV to 0.50 eV (Fig. 1e, f). The three Zn atoms on the defect surface lose 0.62, 0.94, and 0.94 e, respectively. These values are less than those of 1.16, 1.21, and 1.21 e on the pristine surface (Fig. 1a, b). This suggests partial reduction of Zn and enhanced metallic character. Together, these results indicate that OV formation induces the aggregation of surrounding Zn ions into a metallic Zn$_3$ cluster-like structure, and herein we refer to this structural motif as OV-Zn$_3$.

3.2 H atomic adsorption

We investigated eight adsorption structures of a single H. When the H atom is adsorbed on the Zn atoms (Fig. S4b, d, e) or
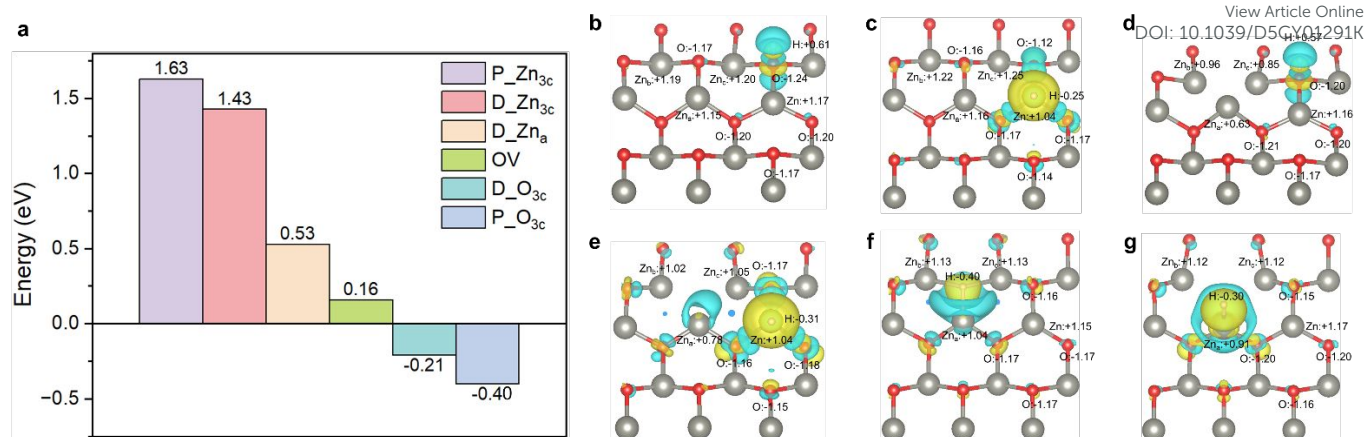
Fig. 2 (a) Adsorption energies of a single H atom at different sites on the pristine and defect ZnO ($10\bar{1}0$) surfaces. (b-g) Charge density difference maps before and after H adsorption at different sites. Yellow indicates electron accumulation, blue represents electron depletion, and the numbers are Bader charges.

at the OV site (Fig. S4f), the charge is localized near the H atom, indicating strong electron transfer characteristic of ionic bonding. In contrast, the charge is localized along the O-H bond (Fig. S4a, c), with the electron cloud more strongly concentrated toward the O, which is characteristic of covalent bonding. The stability of H atomic adsorption at different sites follows the order of pristine surface O_{3c} > defect surface O_{3c} > OV > defect surface Zn_a > defect surface Zn_{3c} > pristine surface Zn_{3c}, and the respective adsorption energies are −0.40, −0.21, 0.16, 0.53, 1.43, and 1.63 eV (Fig. 2a). It is evident that adsorption of a single H atom at the surface Zn_{3c} site is highly unlikely under realistic conditions because of the high endothermic adsorption energy.

The formation of OV-Zn_3 suppresses H adsorption at the O_{3c} site due to the more endothermic adsorption energy, accompanied by the decrease in the charge transfer to the surface from 0.61 e (Fig. 2b) to 0.57 e (Fig. 2d). On the pristine ZnO ($10\bar{1}0$) surface, the O_{3c} atom directly binding the H atom gains only 0.08 e, and the Bader charges of the other atoms change only slightly. Thus, the excess charge is nearly uniformly delocalized over the entire slab, indicating that ZnO possesses a strong capacity for electron storage, consistent with the earlier work of Zhang et al.[58]. Conversely, H adsorption at the Zn_{3c} site is promoted by the presence of OV-Zn_3. When adsorbed at the OV site, the H atom nearly occupies the original O_{3c} position, delocalizing the charge and stabilizing the defect structure (Fig. 2f). The H adsorbate can alternatively be viewed as occurring at the hollow site of the Zn_3 cluster, which acquires significantly more charge from the surface by binding multiple Zn atoms compared to its adsorption at the regular Zn_{3c} or Zn_a site. Thus, H adsorption at the OV site is substantially stronger than that at other Zn sites, as reflected by its notably lower adsorption energy, making it possible for H to adsorb at the OV site under typical experimental conditions.

The formation of OV-Zn_3 markedly alters the interaction between hydrogen and the ZnO ($10\bar{1}0$) surface, especially when H is adsorbed on Zn. On the defect surface, the OV-Zn_3 motif acts as an electron reservoir, characterized by its strong electron-donating ability and relatively weak electron-accepting capacity. Figs. 2e and S4d clearly

reveal the disappearance of localized electron density at the OV site, confirming the role of the OV-Zn_3 motif as a key source of electrons in the charge redistribution process. Changes in the localized charge of the OV-Zn_3 region induced by H adsorption further leads to lattice distortion. H adsorption at an O_{3c} site increases the local electron density at Zn_a and Zn_c, shortening the Zn_a-Zn_c and Zn_b-Zn_c distances while slightly increasing the Zn_a-Zn_b distance. Thus, the Zn_a-Zn_c bond is strengthened with the change of the -ICOHP value from
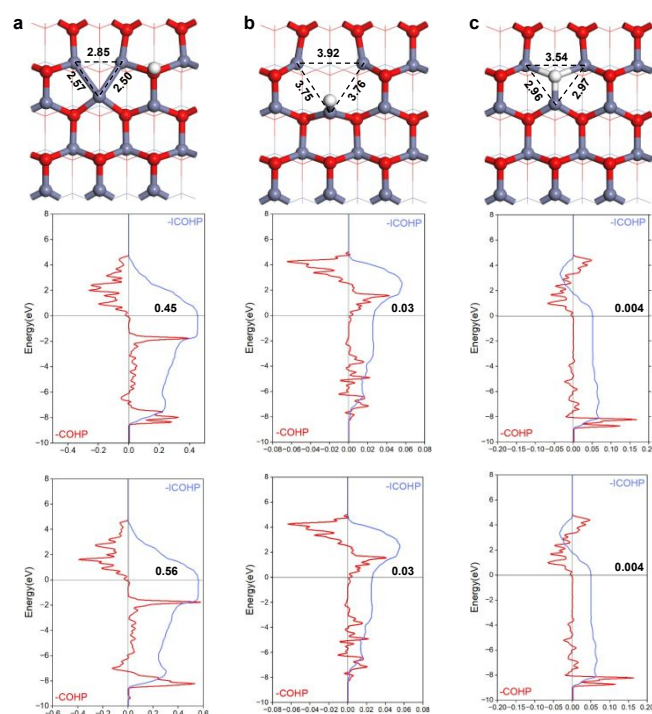

Fig. 3 Lattice distortion around the OV–Zn_3 motif induced by H adsorption: a single H atom at the (a) O_{3c}, (b) Zn_a, and (c) OV sites. The top panel shows the adsorption geometry with annotated Zn–Zn distances, the middle and bottom panels present COHP analyses of the Zn_a–Zn_b and Zn_a–Zn_c bonds.

0.50 eV to 0.56 eV, whereas the Zn_a-Zn_b bond is weakened with the -ICOHP value changing from 0.50 eV to 0.45 eV (Fig. 3a). In contrast, when an H atom adsorbs on Zn_a (Fig. 3b), depletion of the localized electron density increases electrostatic repulsion among the Zn cations, driving their further separation. Accordingly, the –ICOHP value between Zn_a and Zn_b (or Zn_c) decreases from 0.50 eV to 0.03 eV. When H adsorbs at the OV site (Fig. 3c), local electrons are likewise depleted. The Zn–Zn separations become shorter, and the system is stabilized, because the H atom simultaneously coordinates to all three Zn atoms.

3.3 Co-adsorption of H atoms

Fig. 4a demonstrates a pronounced cooperative effect between neighbouring H atoms adsorbed at Zn-O pairs along the [0001] direction. After pre-adsorption of an H atom at the O_{3c} site, adsorption of a second H atom at the dimer-Zn_{3c} site becomes thermodynamically more favourable. The adsorption energies of -0.08 eV and -0.20 eV on the pristine and defect surfaces, respectively. These values are much lower than those of 1.63 eV and 1.43 eV for H adsorption on the clean surface without the pre-adsorbed H. Similarly, H pre-adsorbed at a Zn_{3c} site makes H adsorption on dimer-O_{3c} more exothermic, with adsorption energies of -2.11 eV and -1.85 eV on the pristine and defect surfaces, respectively, compared to those of -0.40 eV and -0.21 eV on the clean surfaces. The adsorption of a second H atom at the trench-O or trench-Zn site is also facilitated by H pre-adsorption on either Zn or O atoms of both pristine and defect surfaces, with corresponding adsorption energies of -1.86, 0.17, -1.64, and 0.00 eV, respectively (Fig. 4a).

In addition to tuning the adsorption energies, H co-adsorption induces significant charge redistribution and affects interfacial bonding. On the defect ZnO $(10\bar{1}0)$ surface, upon the adsorption of an additional H atom at a dimer- or trench-O site, the pre-adsorbed H on O gains some extra electron, 0.05 e and 0.08 e, respectively (Fig. 2e and Fig. 4c, d). Conversely, if the second H adsorbs at a dimer- or trench-Zn site, the pre-adsorbed H on O may lose some electron, 0.00 e and 0.05 e (Fig. 2d and Fig. 4e, f), respectively. Thus, the co-adsorption results in an additional electron transfer from the O-bound H to the Zn-bound H, as visualized by charge-density difference maps (Fig. 4c-f). Compared to single H adsorption, co-adsorption of two H atoms n a Zn-O dimer of the defect surface affects the bond significantly. The H-O bond is weakened, as reflected by a decrease in the -ICOHP value from 3.83 to 3.76 eV (Fig. S5a, b). Conversely, the H-Zn bond is strengthened , with the -ICOHP increasing from 0.96 to 1.00 eV (Fig. S5c, d). Similar trends are also observed on the pristine surface (Figs. S6, and S7). Thus, co-adsorption of two H atoms facilitates additional electron transfer from H-O to H-Zn, weakening the former and strengthening the latter. In addition to electron redistribution, the electrostatic attraction between the oppositely charged H atoms further enhances the stability of the co-adsorption configuration.

When two H atoms are co-adsorbed on adjacent Zn-O pairs, the adsorption of a third H atom at a neighbouring site remains thermodynamically promoted (Fig. 4b), although this effect is notably weaker than that observed for single H pre-adsorption. For the defect surface, when two H atoms are co-adsorbed on a Zn-O dimer (Fig. S8), the adsorption energies of a third H atom at the adjacent O_{3c} or Zn_{3c} site along the [0001] direction are -0.36 eV and 1.36 eV, respectively. If the two H atoms are co-adsorbed on a Zn-O trench, the adsorption energies of a third H at the adjacent O and Zn sites (Fig. S9) along the [0001] direction are -0.57 eV and 0.92 eV, compared to the values of -0.21 eV on O and 1.43 eV on Zn for the clean surface. The pristine surface exhibits the same promotional effect (Figs. S10-S12), indicating that this phenomenon is independent of the presence of oxygen vacancies.
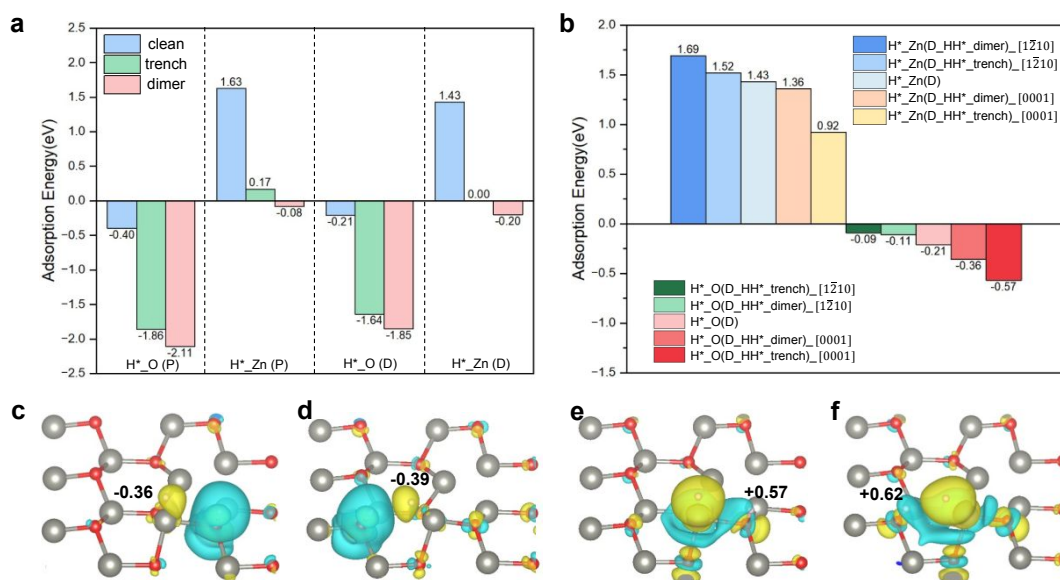

Fig. 4 (a) H adsorption energies at the O or Zn site over the pristine and defect surfaces with three initial states: no pre-adsorbed H (blue), one H adsorbed at the trench site (green), and one H adsorbed at the dimer site (pink). (b) Adsorption energies of the next H atom on the adjacent Zn or O atom along the $[1\bar{2}10]$ and [0001] directions after pre-adsorption of H_2 at the Zn-O dimer or trench, the defect surface without pre-H is shown for comparison. (c-f) Charge density difference maps for adsorption of a second H atom at the dimer-O (c), trench-O (d), dimer-Zn (e), and trench-Zn (f) sites on the defect ZnO $(10\bar{1}0)$.

ARTICLE

It is also evident that H atoms preferentially co-adsorb in pairs on the Zn-O dimer rather than on the Zn-O trench along the [0001] direction. As shown in Fig. 4a, the adsorption of a second H atom on a dimer site (O or Zn) is more exothermic than on a trench site. Furthermore, Figs. 4b and S10 reveal that when two H atoms are pre-adsorbed on a Zn-O trench, the adsorption of an additional H atom is even more exothermic than when the two are on a dimer. This is because co-adsorption on a Zn-O dimer results in isolated trench sites, while co-adsorption on a Zn-O trench leads to isolated dimer sites, which are more favourable for subsequent H adsorption.

Indeed, the next H atom preferentially adsorbs at a neighbouring site along the [0001] direction, rather than along the [1$\bar{2}$10] direction. For the pristine surface, when a single H atom is adsorbed at an O or Zn site, the adsorption energy for a second H atom on the same type of site along the [1$\bar{2}$10] direction is 0.19 eV and 1.79 eV, while these values are 0.28 eV and 0.55 eV for the defect surface, respectively (Fig. S13). Similarly, on the defect surface with a pre-adsorbed H pair on a Zn-O dimer, the adsorption energies for the third H atom on the adjacent Zn and O sites along the [1$\bar{2}$10] direction are 1.69 eV and -0.11 eV, while for that with a pre-adsorbed H pair on a Zn-O trench, these values are 1.52 eV and -0.09 eV (Fig. 4b, S8-S10). These less favourable adsorption energies may be attributed to electrostatic repulsion between adjacent hydrogen atoms of the same polarity along the [1$\bar{2}$10] direction.

3.4 H$_2$ activation and hydrogen chain growth

The chemisorption energies of H$_2$ at the Zn-O dimer sites on the pristine and defect ZnO (10$\bar{1}$0) surfaces are -0.48 eV and -0.42 eV, respectively, closely matching the experimental value of -0.52 eV[59]. In contrast, chemisorption at the Zn-O trench sites is less exothermic, with values of -0.23 eV and -0.21 eV. However, the energy barriers of heterolytic dissociation are higher at the dimer sites, both at 0.52 eV, while those at the trench sites are lower, at 0.21 eV for the pristine surface and 0.19 eV for the defect surface (Fig. 1d and 5a). Thus, H$_2$ activation is kinetically more favourable at the Zn-O trench, despite being thermodynamically more favourable for the adsorption at the Zn-O dimer. Due to the distinct nature of the adsorption sites, this does not contradict the Brønsted-Evans-Polanyi (BEP) relationship[60]. Fig. S15 shows that H$_2$ chemisorption at both dimer and trench sites does not induce charge delocalization at the vacancy, and the activation primarily involves the adsorption site and its nearby atoms. Energetic and electronic structure analyses indicate that H$_2$ activation is nearly identical on the pristine and defect surfaces, which can be attributed to the stabilizing effect of H adsorption at the O$_{3c}$ sites, preserving the electronic and structural integrity of the OV-Zn$_3$ motif. The possibility of H$_2$ dissociative adsorption at the subsurface Zn$_{4c}$ and O$_{4c}$ sites is also studied. We estimated its energetics by AIMD sampling because the hypothetical dissociation state is very unstable and cannot be effectively studied by routine structural optimization. Placing a pair of H atoms at appropriate initial distances on the Zn$_{4c}$–O$_{4c}$ dimer site and on the Zn$_{4c}$–O$_{4c}$ trench, the H atoms recombined into H$_2$ after only 13 fs and 18 fs, with reaction energies of −3.55 eV and −4.69 eV (Fig. S3b, c), respectively. This indicated that dissociative adsorption of H$_2$ at subsurface Zn$_{4c}$ and O$_{4c}$ sites is unlikely to occur under typical experimental conditions.
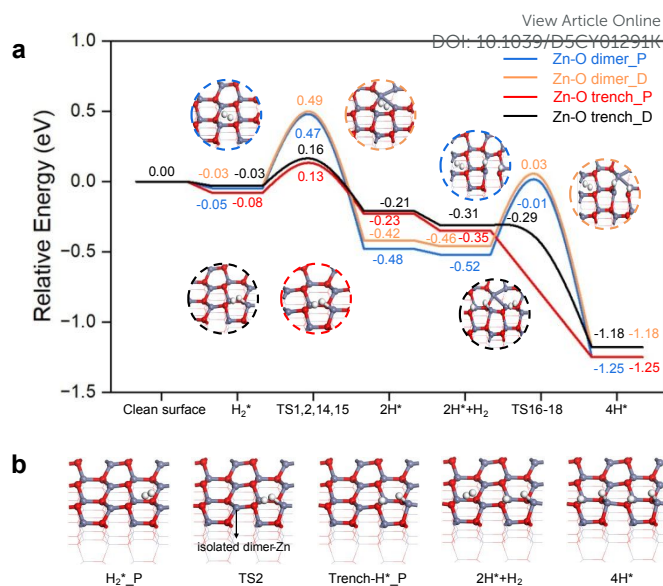
Fig. 5 (a) PES for sequential H$_2$ dissociation at Zn–O dimer and trench sites along the [0001] direction on the pristine and defective ZnO (10$\bar{1}$0) surfaces. (b) Optimized structures along the reaction pathway of consecutive H$_2$ dissociation at the Zn–O trench sites on the pristine ZnO (10$\bar{1}$0) surface.

As discussed in the previous section, H atoms preferentially adsorb along the [0001] direction, leading to the experimentally observed 1D hydrogen chains[32, 37]. We simulated the growth of hydrogen chains by calculating the sequential chemisorption of two H$_2$ molecules along the [0001] direction on ZnO (10$\bar{1}$0) surface. As shown in Figure 5a, the chemisorption of the second H$_2$ at the Zn-O dimer is more exothermic (-0.73 eV and -0.72 eV for the pristine and defect surfaces) than the first, but the energy barriers are nearly unchanged at 0.51 eV and 0.49 eV, indicating no significant kinetic effect. In contrast, at the Zn-O trench, dissociation of the second H$_2$ is even more exothermic (-0.90 eV and -0.87 eV for the pristine and defect surfaces) and essentially barrierless (0 and 0.02 eV), suggesting a highly favourable pathway. The significant reduction in the energy barrier is primarily attributed to the isolated dimer-O and dimer-Zn sites formed by H$_2$ chemisorption at the Zn-O trench (Figs. 5b, S16a, S17a). These isolated dimer O and Zn sites provide stronger binding sites for H atoms from subsequent H$_2$ dissociation, thereby facilitating continuous H$_2$ activation and hydrogen chain growth. In contrast, isolated trench-O and trench-Zn sites (Figs. S18a, S19a) formed by H$_2$ adsorption at the Zn-O dimer have much lower affinity for additional H atoms and do not markedly promote sequential H$_2$ dissociation, consistent with the discussion in the previous section. Besides, the dissociative adsorption of a second H$_2$ molecule along the [1$\bar{2}$10] direction is more difficult (Fig. S16-S20), indicating that hydrogen chain growth along this direction is energetically and kinetically disfavoured. Therefore, hydrogen chains grow continuously only along the [0001] direction but is discontinuous along the [1$\bar{2}$10] direction, resulting in their characteristic one-dimensional morphology.

We note that diffusion may occur due to the varying adsorption strengths of H at different sites. In fact, the H atoms adsorbed in pairs on the Zn$_{3c}$-O$_{3c}$ site are very stable. When two H atoms are co-

adsorbed on the Zn_{3c}-O_{3c} dimer, the migration of the H on Zn_{3c} to a neighbouring trench-O_{3c} site (Fig. S21c) is endothermic by 0.26 eV with a significant energy barrier of 1.17 eV. Similarly, when two H atoms are co-adsorbed on the Zn_{3c}-O_{3c} trench, the migration of the H on Zn_{3c} to a neighbouring dimer-O_{3c} site (Fig. S21c) is also slightly endothermic by 0.06 eV with an energy barrier of 1.13 eV (Fig. S22). These results demonstrate that when an H atom is co-adsorbed at an adjacent O site (dimer-O or trench-O), its migration from neighbouring Zn_{3c} becomes thermodynamically and kinetically more difficult, which can be attributed to the cooperative effect of co-adsorption as mentioned earlier, resulting in the 1D hydrogen chains. This is different from the conclusion of Song et al., who believed that even if H atoms are adsorbed in pairs, H on Zn_{3c} could easily migrate to adjacent O_{3c} atoms[34]. In fact, early infrared studies of H_2/D_2 chemisorption on predominantly $(10\bar{1}0)$-terminated ZnO already revealed type-I hydrogen species, where the Zn–H stretching modes appear along with the characteristic O–H bands, attributed to heterolytic H_2 dissociation at the Zn–O pairs[61]. Further high-resolution FTIR "spectral-ratio" measurements identified weak absorptions near 840 and 820 cm^{-1} attributable to coupled δ(OH) and δ(ZnH) bending modes[62], while incoherent inelastic neutron-scattering studies identified Zn–H bending and stretching modes around 829 and 1708 cm^{-1}, in excellent agreement with the IR experiment[63]. More recent DRIFTS/INS studies[64] and theoretical analyses further confirmed this picture, consistently treating type-I Zn–H hydrides associated with Zn–O pairs as experimentally detectable but minor H species on ZnO surfaces. This also shows that H species on Zn_{3c} do not completely migrate to O_{3c} atoms.

In addition to the regular Zn_{3c}-O_{3c} sites, H_2 can also be activated at OV-Zn_3. We examined seven possible dissociation pathways involving this site (Fig. S23, Table S1). Unlike H_2 activation at the Zn_{3c}-O_{3c} sites, where the vacancy plays a negligible role, here the OV-Zn_3 motif directly mediates H_2 activation (Table S2). Among these pathways, the heterolytic dissociation of H_2 across Zn_a and O_{3c} along the [0001] direction is endothermic by 0.17 eV but exhibits the lowest energy barrier of 0.60 eV, rendering it kinetically the most favourable (Table S1 and Fig. S24). Additionally, H_2 dissociation between the OV and Zn_a sites is slightly exothermic by -0.10 eV, yielding the thermodynamically most stable configuration, but involving a high energy barrier of 1.42 eV. Another pathway, involving H adsorption at the Zn_a-Zn_b and Zn_a-Zn_c bridge sites—resembling homolytic H_2 dissociation on metal surfaces—is both kinetically (2.79 eV) and thermodynamically (1.39 eV endothermic) unfavourable. ELF and Bader charge analyses (Fig. S25) confirm the homolytic nature of both processes. The remaining four pathways are all exothermic with energy barriers exceeding 1.00 eV. These results show that H_2 activation at OV-Zn_3 is clearly more difficult than that at Zn_{3c}-O_{3c}, which can proceed even at temperatures as low as 20 K[32], but that at OV-Zn_3 requires high temperatures. Since reactions such as CO_2 hydrogenation to methanol typically occur at 473-573 K[65-69], this makes H_2 activation at OV-Zn_3 possible under typical experimental conditions for these reactions.

3.5 Regulation of H$_2$ activation and diffusion by reaction conditions

H_2 can dissociate through multiple pathways at different sites on the defect ZnO $(10\bar{1}0)$ surface followed by H diffusion. Consequently, the surface coverage of hydrogen species can vary with the reaction

conditions. Based on our studies on H_2 activation and diffusion, we rationalize the experimental observation of Song et al.[34] that H species can be clearly observed at OVs at 200 °C, whereas further increasing the temperature to 300 °C leads to a decrease in H coverage at OVs.

At a low temperature, the OV concentration on the ZnO $(10\bar{1}0)$ surface is negligible, and the 1D hydrogen chains observed at ~20 K mainly[32] originate from sequential H_2 chemisorption at adjacent Zn-O trenches. Upon heating to 423 K, low concentrations of OVs are formed. However, due to the relatively high energy barrier for H_2 dissociation at the OV-Zn_3 sites, OV-mediated H_2 activation is unfavourable at a low OV concentration. Once the temperature reaches ~473 K, homolytic H_2 dissociation at OV-Zn_3 to form H atoms adsorbed at the OV and Zn_a sites becomes kinetically favourable, considering the size of its energy barrier of 1.43 eV. This leads to the emergence of the characteristic ^{1}H MAS NMR resonance at ~8.4 ppm assigned to hydride species located at OVs, accompanied by a concurrent decrease in the EPR intensity and the O 1s XPS signal associated with paramagnetic OVs[34].

The co-adsorption of two H atoms at the OV and Zn_a sites remains relatively stable within a certain temperature range. As shown in Fig. 6, we examined two possible pathways for the transformation of this co-adsorption configuration into a thermodynamically more favourable state, namely, a pair of H atoms adsorbed on a Zn-O dimer. In pathway I (Fig. 6c), H on Zn_a migrates along the [1$\bar{2}$10] direction to Zn_{3c} with an energy barrier of 0.86 eV, followed by the migration of another H at OV to O_{3c} with a much higher energy barrier of 1.57 eV as the rate-determining step. In pathway II (Fig. S26), the H atom at the OV site first migrates to the O_{3c} atom with an energy barrier of 2.10 eV, followed by H migration from Zn_a to Zn_{3c} with an energy barrier of 0.25 eV. Clearly, pathway I is kinetically more favourable, although the energy barrier of its RDS still exceeds that of H_2 dissociation at the OV-Zn_a site. Besides, the intermediate state is less stable than the initial co-adsorption state by 0.57 eV. Thus, the forward process is unlikely to occur unless at elevated temperatures, which enable the two H atoms to sequentially diffuse along the [1$\bar{2}$10] direction to the Zn-O dimer and form the thermodynamically more stable configuration. Within a temperature window, H species can accumulate at the OV–Zn_3 motif rather than fully migrating to the O_{3c}–Zn_{3c} dimers. In addition, H species adsorbed at the OV–Zn_3 motif are unlikely to recombine into H_2 and desorb, because the recombined state is thermodynamically less stable than the co-adsorbed state. Upon further increasing the temperature, more H species initially on OV–Zn_3 can diffuse to the O_{3c}–Zn_{3c} sites via pathway I with an energy barrier only 0.14 eV higher than that of H_2 dissociation at the OV–Zn_3 site. We note that Song et al. further showed that when at 573 K (300 °C), the ^{1}H MAS NMR signal at ~8.4 ppm attributed to H species at OVs becomes weaker than the signal observed after H_2 treatment at 473 K (200 °C)[34]. Our microkinetic simulations based on the above analysis successfully reproduce this behaviour and explicitly reveal the decrease in H coverage at the OV sites (Fig. 6b). Thus, the outward migration mechanism of H atoms at the OV–Zn_3 motif proposed here can explain the experimentally observed decrease, in addition to the bulk O replenishment of surface OV sites proposed by Song et al.[34]

H_2 chemisorption onto the two bridge sites of Zn_3 (i.e., Zn_a-Zn_b
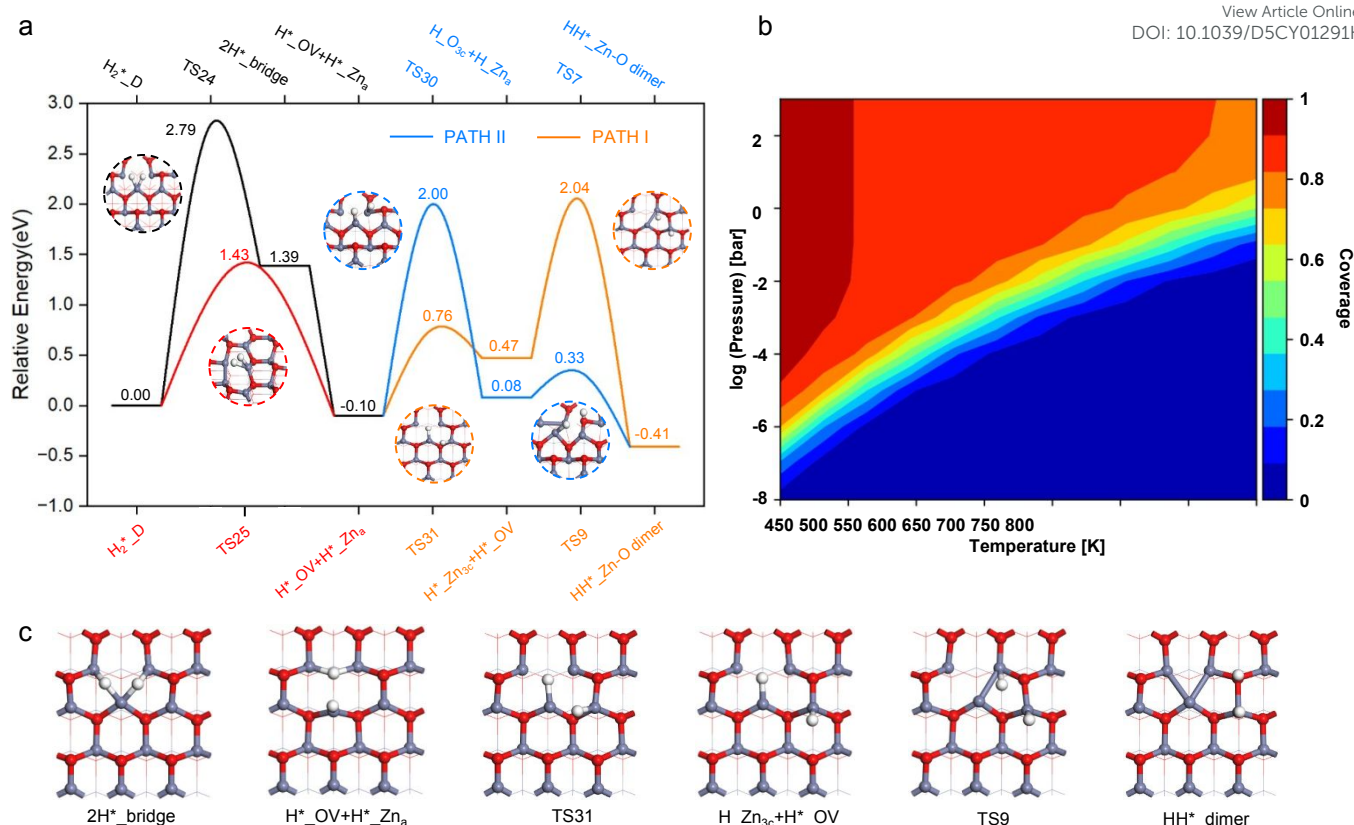
Fig. 6 (a) PES for H_2 dissociation and diffusion at the OV–Zn_3 site: black line represents H_2 dissociation at two bridge sites of the Zn_3 cluster, the red line corresponds to direct H_2 dissociation and adsorption at the OV and Zn_a atoms, the pink and blue lines represent two distinct hydrogen diffusion pathways. (b) The coverage of H species at OV varies with temperature and pressure (c) Key intermediates along pathway I.

and Zn_a-Zn_c) is unlikely to occur under typical reaction conditions, due to the very high energy barrier of 2.79 eV. Even if it occurs at much higher temperatures, the resulting species will spontaneously convert into a more stable configuration without any kinetic barrier, where the two H atoms are co-adsorbed at the OV and Zn_a sites. These H atoms can subsequently diffuse along pathway I to a Zn-O dimer, where they can recombine and desorb as H_2. We also considered H diffusion from the OV and Zn_a sites along the [0001] direction (Fig. S27). Although the RDS has a much lower energy barrier of 1.30 eV, the final states are thermodynamically unstable, making the reverse process kinetically and thermodynamically more favourable (Fig. S28). Therefore, the observed decrease in the H coverage at the OV sites should be primarily attributed to the diffusion of H adsorbates along the [1$\bar{2}$10] direction. In addition to the previous reports on the migration of H atoms from Zn_{3c} to O_{4c}, we also considered the possible migration of H species from Zn_a to O_{4c}. Our simulations show that upon H adsorption on O_{4c}, it pulls O_{4c} from the subsurface to the surface. This was also observed in the "Heterolytic-1 + Migration-1 pathways" of the early work[34]. Our calculations show that the energy barrier for the direct migration of H species from Zn_a to Zn_{3c} is lower than that to O_{4c}, because the former does not involve a high energy for pulling O_{4c} from the deep subsurface to the surface (Fig. S29).

Conclusions

In this study, H_2 activation, formation of the OV-Zn_3 motif, and diffusion of surface H adsorbates on the ZnO (10$\bar{1}$0) surface were investigated by DFT calculations. Our calculations show that H_2 adsorption at the Zn-O trench sites is the most favourable for the formation of the OV-Zn_3 motif, which possesses strong electron-donating ability and relatively weak electron-storage capacity. In addition, H adsorbates at the OV or O site stabilize the defect structure, whereas those on the Zn site induce electron transfer from the OV, leading to an increasing Zn_3 separation. Pre-adsorbed H species can accelerate H_2 dissociation at neighbouring sites, and H atoms preferentially align along the [0001] direction, yielding the experimentally observed 1D hydrogen chains. Our DFT calculations indicate that H_2 dissociation at the OV–Zn_3 motif and the accumulation of H species at the OVs become feasible only at elevated temperatures. However, at higher temperatures, migration of these H species toward the Zn_{3c}–O_{3c} dimers leads to a gradual decrease in the H coverage at Ovs. Our theoretical insights are consistent with the experimental observations, and are further confirmed by our microkinetic simulations.

Our simulations highlight the critical role played by the OV-Zn₃ motif in governing the interaction between the hydrogen species and the surface. The insights gained from this study offer an important perspective for the rational design of ZnO-based hydrogenation catalysts by leveraging defect engineering and thermal control to modulate lattice distortion, hydrogen activation sites, and the directional spillover of hydrogen species.

Author Contributions

Zezhong Miao carried out the theoretical calculations, analysed the data and wrote the initial draft. Xing Zhu assisted with the calculations and data analysis. Yuqian Jin contributed to manuscript editing and discussion. Lingzhao Kong provided scientific advice and guidance, and contributed to the discussion, review and editing of the manuscript. Shenggang Li proposed the project, provided the funding and the research platform, and offered overall guidance as well as critical revision, editing and final approval of the manuscript.

Conflicts of interest

There are no conflicts to declare.

Data availability

The data supporting this article have been included as part of the ESI.†

Acknowledgements

References

1. S. S. Ali, S. S. Ali and N. Tabassum, *Journal of Environmental Chemical Engineering*, 2022, **10**, 106962.
2. S. Kattel, P. J. Ramírez, J. G. Chen, J. A. Rodriguez and P. Liu, *Science*, 2017, **355**, 1296–1299.
3. E. C. Ra, K. Y. Kim, E. H. Kim, H. Lee, K. An and J. S. Lee, *ACS Catalysis*, 2020, **10**, 11318–11345.
4. E. Alper and O. Yuksel Orhan, *Petroleum*, 2017, **3**, 109–126.
5. E. S. Rubin, J. E. Davison and H. J. Herzog, *International Journal of Greenhouse Gas Control*, 2015, **40**, 378–400.
6. F. Jiao, J. Li, X. Pan, J. Xiao, H. Li, H. Ma, M. Wei, Y. Pan, Z. Zhou, M. Li, S. Miao, J. Li, Y. Zhu, D. Xiao, T. He, J. Yang, F. Qi, Q. Fu and X. Bao, *Science*, 2016, **351**, 1065–1068.
7. J. Wang, G. Li, Z. Li, C. Tang, Z. Feng, H. An, H. Liu, T. Liu and C. Li, *Science Advances*, 2017, **3**, e1701290.
8. X. Liu, M. Wang, C. Zhou, W. Zhou, K. Cheng, J. Kang, Q. Zhang, W. Deng and Y. Wang, *Chemical Communications*, 2018, **54**, 140–143.
9. X. Liu, M. Wang, H. Yin, J. Hu, K. Cheng, J. Kang, Q. Zhang and Y. Wang, *ACS Catalysis*, 2020, **10**, 8303–8314.
10. J. Su, D. Wang, Y. Wang, H. Zhou, C. Liu, S. Liu, C. Wang, W. Yang, Z. Xie and M. He, *ChemCatChem*, 2018, **10**, 1536–1541.
11. N. Li, F. Jiao, X. Pan, Y. Chen, J. Feng, G. Li and X. Bao, *Angewandte Chemie International Edition*, 2019, **58**, 7400–7404.
12. H. Yang, Z. Wei, J. Zhang, Y. Dang, S. Li, X. Bu, Z. Zhou, C. Gong, H. Wang, J. Li, Y. Liu, Y. Yang, T. Xiao, C. Liu, Y. Sun and P. Gao, *Chem*, 2024, **10**, 2245–2265.
13. H. Su, Y. Hu, H. Feng, L. Zhu and S. Wang, *ACS Sustainable Chemistry & Engineering*, 2022, **11**, 578–586.
14. Z. Sun, K. Wang, Q. Lin, W. Guo, M. Chen, C. Chen, C. Zhang, J. Fei, Y. Zhu, J. Li, Y. Liu, H. He and Y. Cao, *Angew Chem Int Ed Engl*, 2024, **63**, e202408561.
15. J. Zhao, B. Liu, L. Xiong, W. Liu, D. Wang, W. Ma, L. Jiang, J. Yang, P. Wang, T. Xiao, S. Zhao, P. P. Edwards and J. Tang, *Nat Commun*, 2025, **16**, 1726.
16. R. Huang, C. Liu, K. Zhang, J. Jiang, Z. Tian, Y. Chai and K. Wang, *Nanomicro Lett*, 2025, **18**, 5.
17. Y. R. Shao, L. Zhou, L. Yu, Z. F. Li, Y. T. Li, W. Li and T. L. Hu, *ACS Appl Mater Interfaces*, 2022, **14**, 17195–17207.
18. M. Behrens, F. Studt, I. Kasatkin, S. Kühl, M. Hävecker, F. Abild-Pedersen, S. Zander, F. Girgsdies, P. Kurr, B.-L. Kniep, M. Tovar, R. W. Fischer, J. K. Nørskov and R. Schlögl, *Science*, 2012, **336**, 893–897.
19. S. Kuld, M. Thorhauge, H. Falsig, C. F. Elkjær, S. Helveg, I. Chorkendorff and J. Sehested, *Science*, 2016, **352**, 969–974.
20. X. Xin, P. Gao and S. Li, *Catalysis Science & Technology*, 2024, **14**, 5439–5449.
21. J. Wang, S. Li, W. Liu, Y. Xiao, Z. Feng, X. Liang, S. Tang, G. Li, C. Dong, F. Pan and C. Li, *CCS Chemistry*, 2024, **0**, 1–26.
22. Z. Feng, C. Tang, P. Zhang, K. Li, G. Li, J. Wang, Z. Feng and C. Li, *Journal of the American Chemical Society*, 2023, **145**, 12663–12672.
23. X. Zhang, G. Zhang, W. Liu, F. Yuan, J. Wang, J. Zhu, X. Jiang, A. Zhang, F. Ding, C. Song and X. Guo, *Applied Catalysis B: Environmental*, 2021, **284**, 119700.
24. J. Ye, C. Liu, D. Mei and Q. Ge, *ACS Catalysis*, 2013, **3**, 1296–1306.
25. Y. Liu, T. Zhang, S. Yang, K. Sun, H. Yan, X. Feng, C. Yang and N. Yan, *ACS Catalysis*, 2023, **13**, 16126–16135.
26. T. Zhang, H. Yan, Z. Liu, W. Zhan, H. Yu, Y. Liao, Y. Liu, X. Zhou, X. Chen, X. Feng and C. Yang, *ACS Catalysis*, 2022, **12**, 15181–15192.
27. R. V. Sharma, P. Kumar and A. K. Dalai, *Applied Catalysis A: General*, 2014, **477**, 147–156.
28. S. Basu and A. Dutta, *Materials Chemistry and Physics*, 1997, **47**, 93–96.
29. L. C. Tien, P. W. Sadik, D. P. Norton, L. F. Voss, S. J. Pearton, H. T. Wang, B. S. Kang, F. Ren, J. Jun and J. Lin, *Applied Physics Letters*, 2005, **87**, 222106.
30. K. Anand, O. Singh, M. P. Singh, J. Kaur and R. C. Singh, *Sensors and Actuators B: Chemical*, 2014, **195**, 409–415.

Journal Name

Catalysis Science & Technology Accepted Manuscript

31. N. Al-Hardan, M. J. Abdullah and A. A. Aziz, *Applied Surface Science*, 2009, **255**, 7794–7797.
32. H. Shi, H. Yuan, Z. Li, W. Wang, Z. Li and X. Shao, *The Journal of Physical Chemistry C*, 2019, **123**, 13283–13287.
33. F. Boccuzzi, *Journal of Catalysis*, 1978, **51**, 150–159.
34. B. Song, Y. Li, X.-P. Wu, F. Wang, M. Lin, Y. Sun, A.-p. Jia, X. Ning, L. Jin, X. Ke, Z. Yu, G. Yang, W. Hou, W. Ding, X.-Q. Gong and L. Peng, *Journal of the American Chemical Society*, 2022, **144**, 23340–23351.
35. J. Luo, J.-X. Liu and W.-X. Li, *The Journal of Physical Chemistry C*, 2022, **126**, 9059–9068.
36. B. Song, F. Wang, Q. Zhu, L.-H. Xie and L. Peng, *Chemical Communications*, 2024, **60**, 14121–14124.
37. Y. Ling, J. Luo, Y. Ran, Z. Liu, W.-X. Li and F. Yang, *Journal of the American Chemical Society*, 2023, **145**, 22697–22707.
38. Y. Cao, J. Luo, W. Huang, Y. Ling, J. Zhu, W.-X. Li, F. Yang and X. Bao, *The Journal of Chemical Physics*, 2020, **152**, 074714.
39. C. Guan, X. Yue and Q. Xiang, *Advanced Materials*, 2025, **37**, 2501209.
40. G. Kresse and J. Furthmüller, *Computational Materials Science*, 1996, **6**, 15–50.
41. Efficient iterative schemes for ab initio total-energy calculations using a plane-wave basis set | Phys. Rev. B).
42. J. P. Perdew, J. A. Chevary, S. H. Vosko, K. A. Jackson, M. R. Pederson, D. J. Singh and C. Fiolhais, *Physical Review B*, 1992, **46**, 6671–6687.
43. P. E. Blöchl, *Physical Review B*, 1994, **50**, 17953–17979.
44. G. Kresse and D. Joubert, *Physical review b*, 1999, **59**, 1758.
45. G. Henkelman and H. Jónsson, *The Journal of Chemical Physics*, 2000, **113**, 9978–9985.
46. A dimer method for finding saddle points on high dimensional potential surfaces using only first derivatives | The Journal of Chemical Physics | AIP Publishing).
47. A. Heyden, A. T. Bell and F. J. Keil, *The Journal of Chemical Physics*, 2005, **123**, 224101.
48. A. J. Medford, C. Shi, M. J. Hoffmann, A. C. Lausche, S. R. Fitzgibbon, T. Bligaard and J. K. Nørskov, *Catalysis Letters*, 2015, **145**, 794–807.
49. S. Vijay, H. H. Heenen, A. R. Singh, K. Chan and J. Voss, *Journal of Computational Chemistry*, 2024, **45**, 546–551.
50. R. Materials Studio, Biovia Software Inc., 5005 Wateridge Vista Drive, San Diego, CA 92121 USA.
51. S. Maintz, V. L. Deringer, A. L. Tchougréeff and R. Dronskowski, *Journal*, 2016.
52. K. Momma and F. Izumi, *Journal of Applied Crystallography*, 2011, **44**, 1272–1276.
53. M. Schreyer, L. Guo, S. Thirunahari, F. Gao and M. Garland, *Applied Crystallography*, 2014, **47**, 659–667.
54. H. J. Monkhorst and J. D. Pack, *Physical Review B*, 1976, **13**, 5188–5192.
55. U. Diebold, L. V. Koplitz and O. Dulub, *Applied Surface Science*, 2004, **237**, 336–342.
56. N. R. D'Amico, G. Cantele and D. Ninno, *The Journal of Physical Chemistry C*, 2012, **116**, 21391–21400.
57. Q.-L. Tang and Q.-H. Luo, *The Journal of Physical Chemistry C*, 2013, **117**, 22954–22966.
58. X.-Y. Zhang, Z.-Q. Wang and X.-Q. Gong, *Chemical Science*, 2024, **15**, 13717–13726.
59. A. Dong, L. Lin, R. Mu, R. Li, K. Li, C. Wang, Y. Cao, Y. Ling, Y. Chen, F. Yang, X. Pan, Q. Fu and X. Bao, *ACS Catalysis*, 2022, **12**, 6255–6264.
60. M. G. Evans and M. Polanyi, *Transactions of the Faraday Society*, 1935, **31**, 875–894.
61. F. Boccuzzi, E. Borello, A. Zecchina, A. Bossi and M. Camia, *Journal of Catalysis*, 1978, **51**, 150–159.
62. G. Hussain and N. Sheppard, *Journal of the Chemical Society, Faraday Transactions*, 1990, **86**, 1615–1617.
63. J. Howard, I. J. Braid and J. Tomkinson, *Journal of the Chemical Society, Faraday Transactions 1: Physical Chemistry in Condensed Phases*, 1984, **80**, 225–235.
64. B. Song and L.-H. Xie, *The Journal of Physical Chemistry C*, 2025, **129**, 4825–4840.
65. J. Sehested, *Journal of Catalysis*, 2019, **371**, 368–375.
66. N. D. Nielsen, A. D. Jensen and J. M. Christensen, *Journal of Catalysis*, 2021, **393**, 324–334.
67. K. Lee, U. Anjum, T. P. Araújo, C. Mondelli, Q. He, S. Furukawa, J. Pérez-Ramírez, S. M. Kozlov and N. Yan, *Applied Catalysis B: Environmental*, 2022, **304**, 120994.
68. W. Wang, S. Wang, X. Ma and J. Gong, *Chemical Society Reviews*, 2011, **40**, 3703–3727.
69. J. Graciani, K. Mudiyanselage, F. Xu, A. E. Baber, J. Evans, S. D. Senanayake, D. J. Stacchiola, P. Liu, J. Hrbek and J. F. Sanz, *Science*, 2014, **345**, 546–550.

The data supporting this article have been included as part of the Supplementary

Information.

Catalysis Science & Technology Accepted Manuscript